Plasma Lens for Optical Path Difference Control

Brian W. Neiswander[1] and Eric Matlis[2] and Thomas C. Corke[3]
University of Notre Dame, Notre Dame, IN, 46556.

This research investigated the feasibility of a "plasma lens" for wavefront control of coherent light sources. The approach is based on the relation between a plasma electron density and its index of refraction. The plasma was encapsulated in a hollow glass cylinder with flat optical glass at its ends. Air in the glass cylinder was ionized using a dielectric barrier discharge (DBD). The wavefront distortion produced by the ionized air was characterized by placing the "plasma lens" in one arm of a Michelson interferometer setup. The effect of gas pressure and plasma power were investigated. The results were compared to a derived analytic model that related the electron density and optical path difference (OPD) to the plasma power. The agreement between the experiment and analytic model was very good, especially at the higher plasma power levels. The maximum OPD increased with the gas pressure inside the "lens". A maximum OPD of approximately 1.5 μm was achieved in the experiments. This brackets OPD levels that are typical of aero-optic applications, and otherwise corrected using electro-mechanical deformable mirrors. Although air was used as the gas in the "plasma lens" in these feasibility experiments, the use of Penning mixtures would further increase possible OPD levels and provide greater dynamic range.

---

[1] Ph.D. Student, Aerospace and Mechanical Engineering, B032 Hessert Laboratory, AIAA student member.
[2] Assistant Research Professor, Aerospace and Mechanical Engineering, and AIAA member.
[3] Program Director, Aerospace and Mechanical Engineering, 101 Hessert Laboratory, and AIAA Fellow.

Nomenclature

A = Particle species constant

B = Particle species constant

c = Speed of light

d = Electrode spacing distance

D = Dimensional matrix

ϵ_0 = Electric constant

G = Temperature unit

I = Current

L = Length unit

λ = Laser wavelength

λ_{px} = Interferogram spatial wavelength

j = Counting index

J = Length of time-series data

K = Experimentally determined constant

M = Mass unit

m_e = Electron mass

N = Plasma index of refraction

n_e = Plasma electron density

n_{e0} = Plasma electron density at stable plasma initiation

n_e^* = Plasma electron density dimensional equivalent

n_{heavy} = Heavy particle density at a specific pressure

n_{heavy0} = Heavy particle density at standard temperature and pressure

OPD = Optical path difference

OPD_{px} = Optical path difference in pixels

p = Plasma chamber gas pressure

P = Plasma power

P_{RMS} = Root-mean-square plasma power

P_0 = Power at stable plasma initiation

Π = Pi-group

q = Elementary charge

ϕ = Interferogram phase shift

ϕ_{VI} = Voltage-current phase-angle

R = Individual gas constant

t = Time unit

T = Plasma chamber gas temperature

V = Voltage

ω = Electron optical frequency

ω_P = Plasma frequency

I. Introduction

Directed energy and laser-communications technology in aerospace applications rely on the use of adaptive optics (AO) systems for sufficient energy delivery and data transfer. As a laser's beam passes through shear-layers and turbulence in the wake of a moving aircraft, density gradients can cause distortions, or aberrations, in the beam wavefronts. Aberrations to the laser wavefront are characterized in terms of optical path difference (OPD), which is the integrated effect of changes in index of refraction along the optical path. Wavefront OPDs generated in the near-field significantly reduce the intensity of a beam as it propagates into the far-field[1–3]. When insufficient energy reaches the far-field, OPDs can prevent a target's destruction and inhibit data transfer. A typical range of root-mean-square OPD values in aero-optic applications is 0.025 to 0.15 μm[1].

AO systems utilize closed-loop control schemes to correct for OPDs and restore planar wavefronts. An AO system is typically comprised of a wavefront sensor to measure the OPD, a controller to process and prescribe corrections, and an active wavefront control device to correct for aberrations. An example of an adaptive optic system is shown in Figure 1. The control device is typically a deformable mirror which is a segmented or continuous reflective surface that spatially distorts itself to reflect back planar wavefronts. Deformable mirrors are electro-mechanical devices that have some

inertial limitations. Correction rates typically range from hundreds of Hertz to a few kilo-Hertz. Mechanical deformable mirrors are generally delicate and eventually fail due to material fatigue. Therefore there is a desire to develop more robust wavefront control devices that also might have improved frequency response.
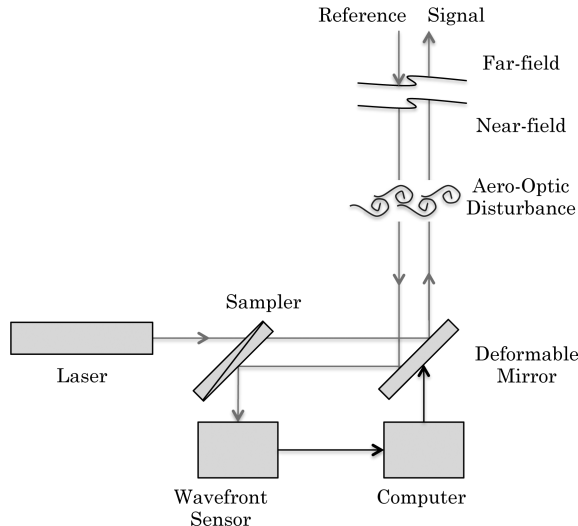

Fig. 1 Schematic of a typical adaptive optics system that uses a deformable mirror.

This research investigates a concept for using ionized gas or plasma, as a dynamic medium to perform wavefront control. Under appropriate conditions, the index of refraction of a plasma varies linearly with its electron density[4]; this relationship is derived later in Section III. Since the plasma electron density can be varied through its applied electric field, this approach can provide a method for dynamically controlling the index of refraction. If the plasma is confined within a volume, it is possible to effectively created a "plasma lens" with a variable index of refraction. The frequency response of such a "plasma lens" is only limited by the recombination time of electrons and ions and therefore should be in the range of hundreds of kilohertz[5, 6]. This would easily exceed by an order of magnitude the fastest deformable mirrors now available.

One concept for an optical wavefront control system could consist of a 2-D array of "plasma lenses" that cover a conventional rigid mirror as shown in Figure 2. The voltage potential to the individual plasma lenses would be individually controlled so that a large-scale spatially-coherent wavefront distortion could be produced. A similar approach is used in plasma-display-panels (PDPs) of plasma televisions, although in that case the light emission property of the plasma is utilized[11],
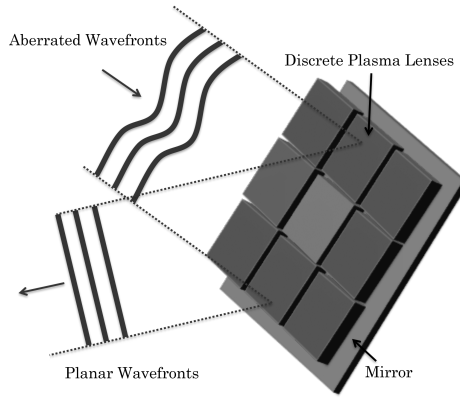
4

Fig. 2 Conceptual plasma wavefront correction device consisting of addressable plasma lenses of uniform electron density that cover the surface of a rigid mirror.

rather than the wavefront distortion property.

Objective. The object of this research was to investigate the feasibility of a "plasma lens" for wavefront control of light sources. The approach would focus on the use of a dielectric barrier discharge (DBD) for the plasma generation. The DBD approach creates a low-temperature, AC gas discharge, that has found numerous uses in other fields of study. General reviews of DBD plasma physics and applications have been given by Corke et al.[7] and Moreau[9]. DBD plasma generation is favorable for this application because it (1) has a high frequency response, (2) has a delayed glow-to-arc transition that allows for a significantly larger voltage operating range compared to DC plasma generation, (3) is easy to adapted to different geometries, and (4) can produce stable plasmas over a large range of pressures[5, 7–10].

The research is intended to characterize the wavefront distortion produced by the DBD generated plasma. This would involve an investigation of the relation between a plasma electron density and its index of refraction as a function of such independent variables as the ionized gas pressure and the plasma power. The wavefront distortion would be measured by placing the "plasma lens" in one arm of a Michelson interferometer. The results would be compared to a derived analytic model that relates the electron density and OPD, to the plasma power.

II.   Experimental Setup

A non-thermal, DBD plasma was generated inside a hollow Pyrex cylinder. A schematic and photograph of the Pyrex cylinder are shown in Figure 3. The Pyrex cylinder was 152 cm in length, 1.9 cm in diameter, and had a wall thickness of 0.28 cm. Both ends of the cylinder were sealed with 2.54 cm diameter, 5 mm thick optical glass disk. The laser beam in the interferometer setup passed through the optical glass ends of the cylinder. A vacuum port with a valve was located halfway along the length of the cylinder. This was connected to a vacuum pump that was used to evacuated the air in the cylinder to a low pressure. Once the pressure was set, the valve closed the port and the vacuum pump was disconnected. Copper tape electrode strips were placed at both ends of the Pyrex tube and wrapped completely around the outer circumference. A high-voltage AC input was applied to the electrodes. The AC waveform was a sine-wave at 14kHz.
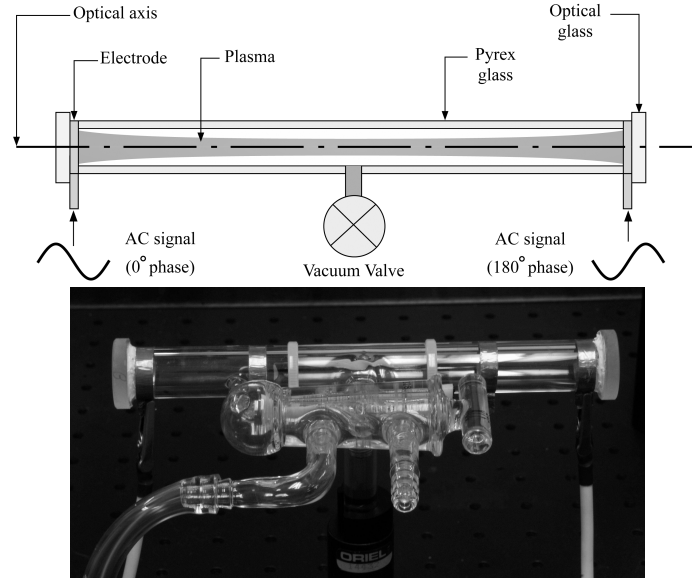

Fig. 3 Schematic (top) and photograph (bottom) of the hollow Pyrex cylinder used as the "plasma lens".

The Pyrex cylinder was located in one arm of a Michelson interferometer that was assembled for the experiments. A schematic of the optical setup is shown in Figure 4. The Pyrex cylinder is labeled "plasma lens" in the schematic. The Michelson interferometer was used to measure the OPD produced by the plasma in the Pyrex cylinder. The OPD is related to the index of refraction of the plasma. The index of refraction is a function of the plasma electron density[4].
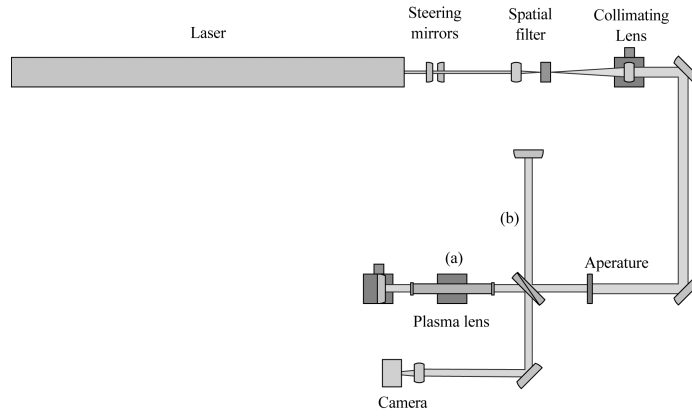
Fig. 4 Schematic of optical path of the Michelson interferometer that was used to measure electron density in the "plasma lens".

The light source used in the optical setup was a 25 mW, 633 nm helium-neon laser. A 8 μm pinhole spatial filter was used to collimate and produce nearly planar wavefronts of the incoming laser. The laser beam split along two paths. The reference path, labeled "b", reflected off the beam-splitter and then was reflected directly back. The measurement path, labeled "a", passed through the beam-splitter and the "plasma lens" and was reflected back. The reflecting mirror in path "a" was placed on a mechanical stage to allow adjustment of the path length. The beams were then recombined and imaged onto a digital camera where the interferograms were stored. Analysis of the interferograms was performed in post-processing.

Experiments were conducted with different gas static pressures inside the Pyrex cylinder. At each pressure, a range of AC voltage amplitudes were applied to cause the air inside Pyrex cylinder to ionize. At each AC voltage, voltage and current time-series data and interferogram images were acquired. A schematic of the automated experiment control and data acquisition system is shown in Figure 5.

A TCP-controlled Agilent 33220A function generator was used to generate the input carrier waveform for the plasma. The function generator output was transformed into a high voltage, low current signal using two Crown XTi4000 amplifiers and two Corona Magnetics transformers. The gas pressure inside the chamber was measured with a Heise H51011 absolute pressure gauge. The voltage potential of the output from one of the transformers was measured with a LeCroy
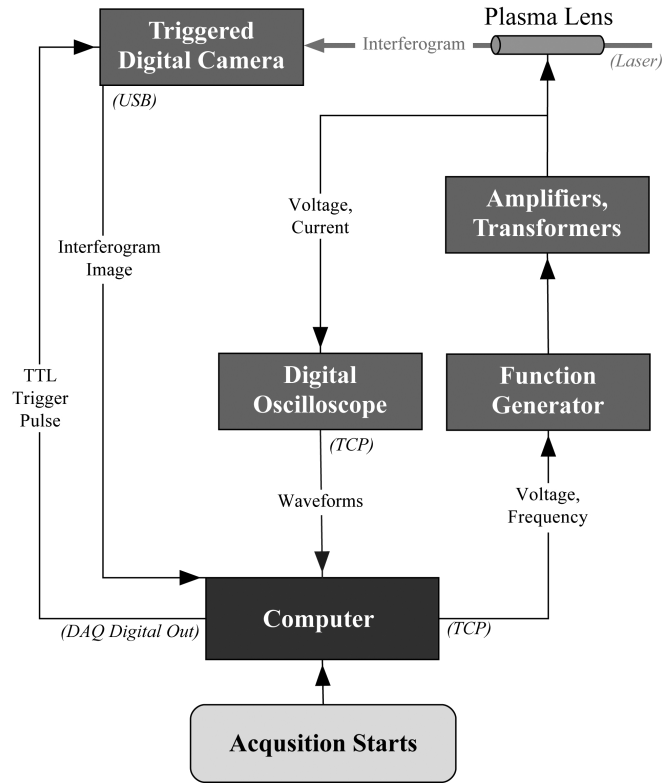
Fig. 5 Schematic of the automated data acquisition and control system used for the "plasma lens" analysis.

PHV4-1903 high voltage probe, and the current is measured with a Pearson 2100 current monitor. Both signals were acquired with a LeCroy WaveRunner LT264 oscilloscope. The oscilloscope's A/D converter has 8-bit resolution and a 1 GHz sampling frequency. Both were suitable for capturing some of the plasma discharge spikes that appeared in the current measurements. Data from the oscilloscope was passed to the computer using a TCP socket connection. Interferograms images were taken with a Spot Image 12-bit, 5-megapixel digital camera. The camera's active sensor size was 5.7mm horizontal by 4.28 mm vertical. A 100 mm lens was placed in front of the camera and adjusted so that the interferogram completely filled the sensor. The camera was triggered with a TTL pulse from the computer.

During data acquisition, the following actions are performed: (1) a TTL trigger was sent to the camera to acquire a reference (voltage-off) interferogram; (2) the computer set the appropriate voltage on the function generator and enabled the output to generate a plasma; (3) a TTL trigger

8

was sent to the camera to capture the active (voltage-on) interferogram; (4) the computer set the appropriate time/voltage scales on the oscilloscope and acquired 12 periods of the current and voltage waveforms; (5) the output to the function generator was turned off; (6) twenty second timeout was performed. This process repeated for a range of function generator voltages.

III.   Results

Two interferograms were recorded (reference and active) for every voltage-pressure combination examined in the experiment. A sample pair of interferograms are shown in Figure 6. The axes are shown in pixels where 1 pixel corresponds to 3.88 nm and the distance between two fringes is equal to the laser's wavelength (633 nm). Image processing techniques were applied to each interferogram image to determine the fringe locations. The shift that occurred in the fringe locations between the cases with the plasma present, and corresponding reference, were used to determine the spatial values of OPD.

The image processing first consisted of cropping the interferograms to a fixed region of interest selected to include the largest rectangular area within the circular interferogram image. A two-dimensional digital filter was then convolved with each image to remove high-frequency noise. The digital filter did not distort the locations of the fringes. The corresponding fringes were then carefully registered between each reference and active image pairs.

Each digitized interferogram consisted of a 2-D matrix of values that were proportional to light intensity. A single matrix row consisted of a sinusoidal light intensity data series with peaks corresponding to bright areas and valleys corresponding to dark areas. The boundary between light and dark areas represented an interferometric fringe. A fringe-tracking algorithm was used to locate the center of each fringe, and keep a count of the fringe numbers. This process was repeated for every row within the interrogation region.

A shift in the position of a specific fringe between the active and reference images corresponds to the local OPD, in pixels. From the pixel-valued OPD, the observed phase shift, ϕ, is found using

$$\phi = \mathrm{OPD_{px}}\frac{2\pi}{\lambda_{px}}, \tag{1}$$

where $\mathrm{OPD_{px}}$ is the OPD in pixels and λ_{px} is the spatial wavelength of the interferograms in pixels.
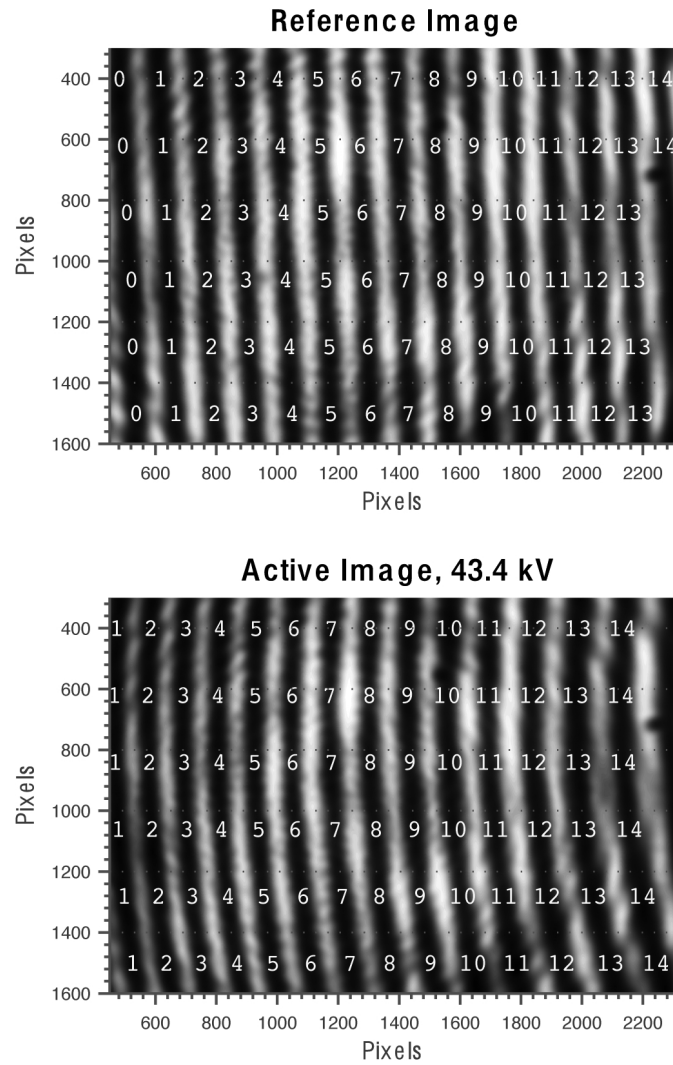
Fig. 6 A sample pair of interferograms obtained in the experiments. The left image is the baseline with the plasma off, and the right image is with the plasma on.

The OPD in physical dimensions is

$$\text{OPD} = \text{OPD}_{\text{px}}\frac{\lambda}{\lambda_{\text{px}}}, \tag{2}$$

where λ is the laser wavelength. For the Michelson interferometer [14, 15], the average refractive index of the "plasma lens" with electrode spacing d is then,

$$N = 1 + \phi\frac{1}{2d}\frac{\lambda}{2\pi}. \tag{3}$$

We were seeking a relation between the plasma electron density and the index of refraction found in the experiments. In this, two frequencies were predominately important: the laser optical

frequency ω, and the plasma frequency ω_P. These are respectively defined in Equations 4 and 5.

$$\omega = \frac{2\pi}{\lambda}c \qquad (4)$$

$$\omega_P = \sqrt{\frac{n_e q^2}{m_e \epsilon_0}} \qquad (5)$$

Here c is the speed of light, n_e the electron density, q the elementary charge, m_e the electron mass, and ϵ_0 the electric constant. The following dispersion equation describes the refractive index due to oscillating free electrons and heavy particles inside a plasma field [4, 12],

$$N = 1 - \frac{\omega_P^2}{2\omega^2} + \left(A + \frac{B}{\lambda^2} \right) \frac{n_{heavy}}{n_{heavy0}}, \qquad (6)$$

where N is the plasma index of refraction, A and B are species constants, and n_{heavy} and n_{heavy0} are the heavy particle densities at a specific and standard pressure, respectively.

Assuming that the heavy particle density is very low, the latter terms in Equation 6 can be neglected. Then the dispersion equation simplifies to

$$N = 1 - \frac{1}{2} \left(\frac{\omega_P}{\omega} \right)^2 . \qquad (7)$$

Equations (4), (5), and (7) can then be combined to give an expression for the electron density, namely

$$n_e = 2(1 - N) \left(\frac{m_e \epsilon_0}{q^2} \right) \left(\frac{2\pi}{\lambda}c \right)^2 . \qquad (8)$$

The instantaneous power of the plasma is the product of current and voltage. For the discrete voltage and current time series collected during the experiments, the power is

$$P = \frac{1}{J} \sum_{j=1}^{J} V_j I_j \qquad (9)$$

where J encloses an integer number of cycles. In the experiment, discrete time series data for the plasma applied voltage and current were recorded for post-calculation of the power. Another quantity of interest is the power level at which stable plasma initiates inside the chamber. This was found from inspection of the phase-angle between voltage and current,

$$\phi_{VI} = \cos^{-1} \left(\frac{P_{RMS}}{P} \right) \qquad (10)$$

11

where P_{RMS} is the root-mean-square of power. Without plasma, the phase shift between the voltage and current remained at about 90°. At the initiation of plasma there was a sudden decrease in phase. From experimental observations it was noted that "stable" plasma did not form until the phase shift was less than about 85°. This was the metric we adopted to ensure that a stable plasma was present during the measurements.

A.   Electron Density Model

A model for the plasma electron density was derived from a Buckingham-Pi analysis[13]. The included variables were power P, electron density n_e, gas pressure p, gas temperature T, and the gas constant R. The five properties are expressed in basic dimensions (mass M, length L, time t, temperature G) given by the following equations.

$$P \doteq ML^2t^{-3} \tag{11}$$

$$n_e \doteq L^{-3} \tag{12}$$

$$p \doteq ML^{-1}t^{-2} \tag{13}$$

$$T \doteq G \tag{14}$$

$$R \doteq L^2t^{-2}G^{-1} \tag{15}$$

The dimensional matrix was constructed and shown below in reduced echelon form.

$$\mathbf{D} = \begin{pmatrix} 1 & 0 & 0 & 0 & 2 \\ 0 & 1 & 0 & 0 & -2 \\ 0 & 0 & 1 & 0 & 4/3 \\ 0 & 0 & 0 & 1 & -1 \end{pmatrix}$$

With five variables and four dimensions, we expected one pi-group. The right null-space vector of the over-determined system $\mathbf{D}$ gave the pi-group,

$$\Pi = \frac{n_e^{4/3}P^2}{p^2RT} \tag{16}$$

We sought some function f such that

$$f(\Pi) = 0. \tag{17}$$

12

A solution was found and written in terms of electron density,

$$n_e = n_{e0} + K \left(p^2 RT\right)^{3/4} \left(\frac{1}{P^{3/2}} - \frac{1}{P_0^{3/2}} \right) \tag{18}$$

where n_{e0} and P_0 are the electron density and power at the initiation point of stable plasma. K is an experimentally determined constant that absorbs information pertaining to the plasma actuator geometry, dielectric properties, and gas ionization properties.

The model predicts the electron density for any subsequent power as a function of the gas pressure or temperature. In particular it shows the weighting (dominance) of each parameter. The model requires knowing the power and electron density at plasma initiation at any pressure of interest, and an experimentally determined constant.

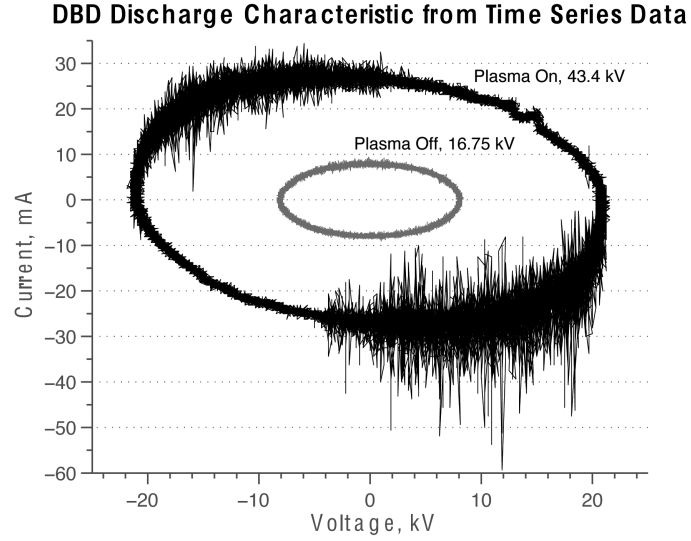**DBD Discharge Characteristic from Time Series Data**

Fig. 7 Sample phase plot of current-voltage data pairs for two different voltages whereby the plasma is (black trace) or is not (red trace) present in the "plasma lens".

IV.   Results and Discussion

Experiments were conducted to validate the electron density model given in Equation 18. This model is the key element in relating the OPD of the plasma lens with the input voltage or plasma power.

Interferograms were collected for three air pressures inside the plasma chamber: 25.86 torr, 33.61 torr, and 41.73 torr. At each pressure, data was taken at 16 different AC voltage levels ranging from
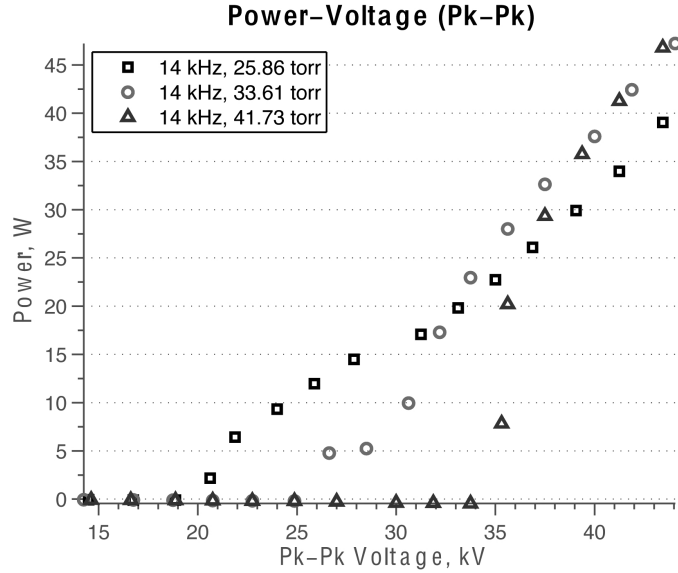
Power-Voltage (Pk-Pk)

Fig. 8 Power-voltage characteristics for the plasma as a function of pressure.

14 to $44\,\mathrm{kV}_{p-p}$. Atmospheric temperature and pressure were recorded before each test. Analysis of the interferogram image pairs provided the OPD, and the index of refraction. Post-analysis of the current and voltage data series was used to determine the power in the analytic model.

Figure 7 shows an example phase plot of voltage-current data series. Each AC cycle forms an approximate ellipse. The phase plot is made up of 12 AC periods. The inner, red ellipse corresponds with a lower AC voltage that was below the level needed to ionize the air. The outer, black ellipse corresponds to an AC voltage that was large enough to ionize the air. This is evident by the high frequency discharge spikes that when averaged, cause an asymmetry in the voltage-current phase plot that when integrated, results in a net power dissipation. The net power was calculated based on Equation 9.

The resulting power as a function of the applied AC voltage level for the three gas pressures is shown in Figure 8. The voltage at which the power begins to increase marks the condition where the air first ionizes. The voltage where this occurs decreases with decreasing pressure. Once the air ionizes, there is an approximately linear relation between voltage and power.

Visual observations of the plasma indicated the possibility of unstable behavior that particularly occurred at lower voltages, just above the minimum needed to ionize the air. The term *stable* is
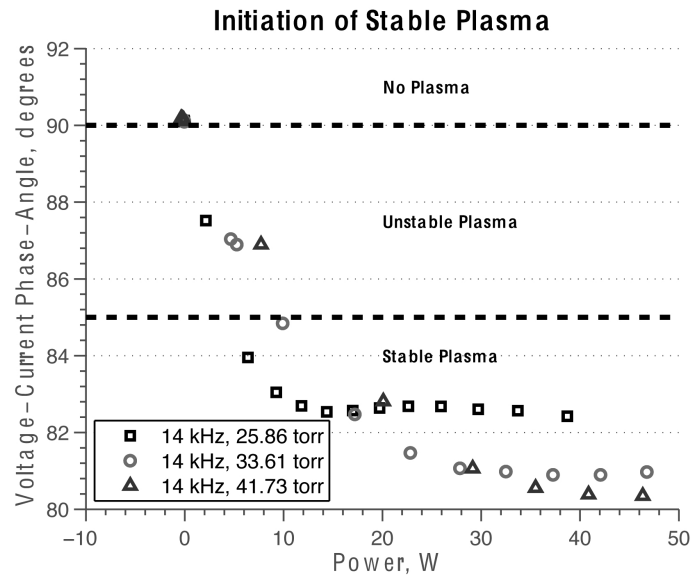
14

Fig. 9 Phase-angle between voltage and current as a function of plasma power for different pressures.

used to describe plasma with no visual transients in it's structure and formation; an *unstable* plasma flickers and can move around within the chamber. A method to identify the region of stable plasma generation involved monitoring the phase angle between the voltage and current. This is plotted as a function of power for the three gas pressures in Figure 9. The horizontal dashed lines indicate boundaries where visual observations indicated that there was no plasma, unstable plasma, or stable plasma. At lower power or voltage levels that were below the minimum needed to ionize the air, the phase angle between the current and voltage was 90°. Once minimum voltage was exceeded, the plasma formed and the phase angle decreased. The phase change was a direct result of a change in the total capacitance of the plasma as it initiated and became stronger. However, observations indicated that the plasma was stable only when the phase angle was less than 85°. Therefore for each of the gas pressures, the plasma initiation power used in the model analysis was the minimum power value at which the voltage-current phase angle was less than 85°.

The OPD values were found from analysis of interferogram image pairs. Spatial OPD maps as a function of the AC voltage for the three gas pressures are shown in Figures 10 to 12. The cylindrical electrode configuration of the "plasma lens" created a spatial gradient of the plasma with highest

electron density in the center. This was observable during the experiments and is quantified in the OPD contours. As the voltage potential increased, the region where the air was ionized increased. This required higher voltages at the higher gas pressures.
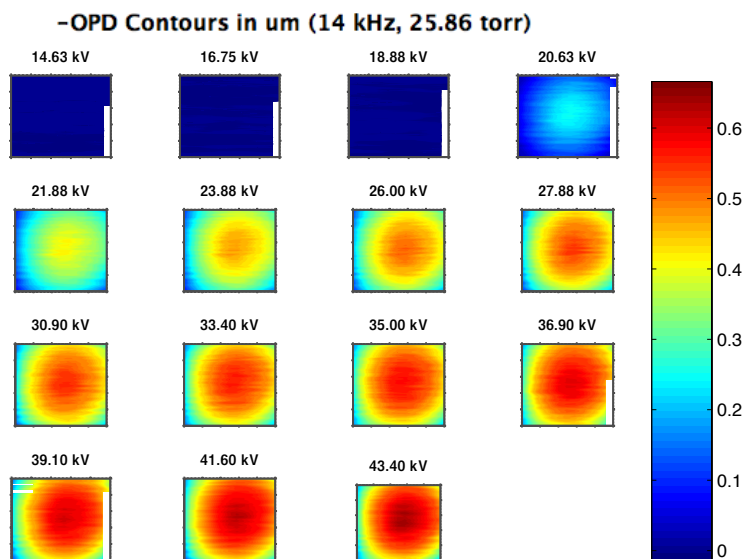
-OPD Contours in um (14 kHz, 25.86 torr)

Fig. 10 Spatial contours of -OPD in 10^{-6} m as a function of voltage for a gas pressure of 25.86 torr.
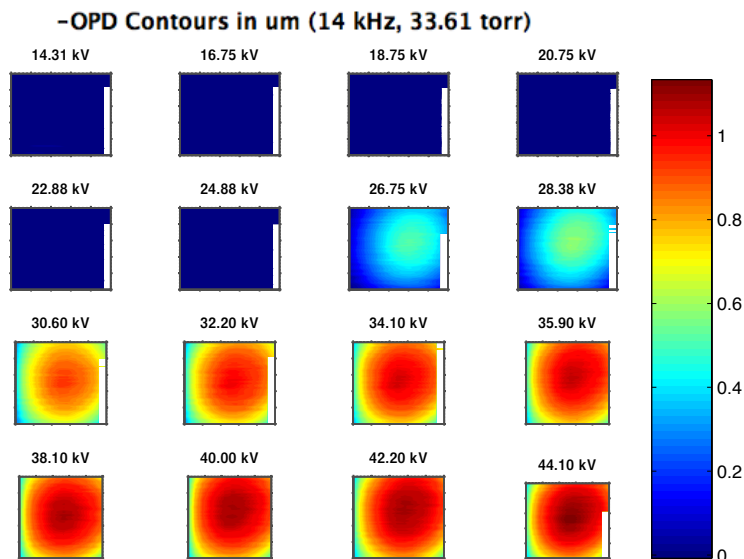
-OPD Contours in um (14 kHz, 33.61 torr)

Fig. 11 Spatial contours of -OPD in 10^{-6} m as a function of voltage for a gas pressure of 33.61 torr.
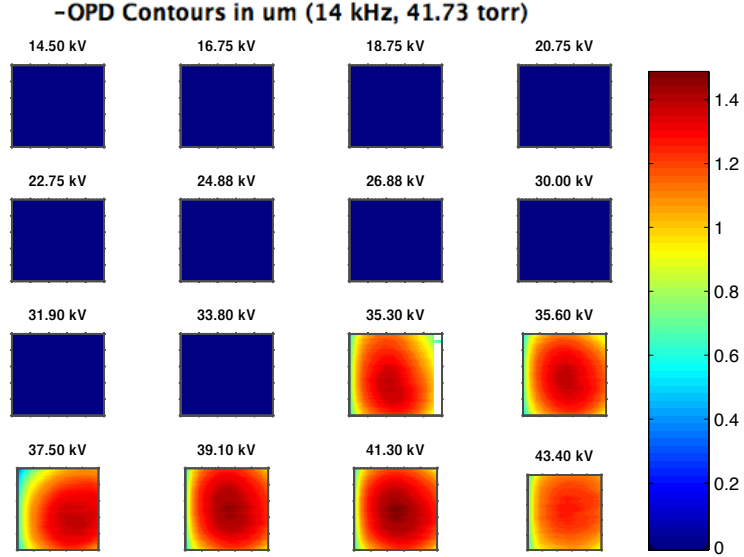
16

Fig. 12 Spatial contours of -OPD in 10^{-6} m as a function of voltage for a gas pressure of 41.73 torr.

The maximum OPD values from each spatial map in Figures 10 to 12 were used to calculate respective electron density values. The results were used with Equations. 1, 2, 3, and 8 to determine the electron density. The electron density and OPD are plotted versus the plasma power in Figure 13 for the three gas pressures. The symbols correspond to the measured values. The curves are based on the analytic model given in Equation 18. The agreement is very good.

A maximum OPD of approximately 1.5 μm was achieved at the highest pressure. This exceeds by an order of magnitude, the OPD values cited in aero-optic applications by Gordeyev et al[1]. The dynamic range of the OPD of the "plasma lens" depends on the plasma power and gas pressure.

Experimental values were required for the electron density model, specifically, the power and electron density values at stable plasma initiation, and the experimental constant K. The former was determined based on the criterion given by Figure 9. For the latter, a new variable, n_e^*, was defined and given as

$$n_e^* = \left(\frac{p^2 RT}{P^2} \right)^{3/4}.$$ (19)

A plot of the electron density, n_e, versus n_e^* should produce a straight line with a slope that corresponds to the experimental constant, K. This is shown in Figure 14. The data at the two
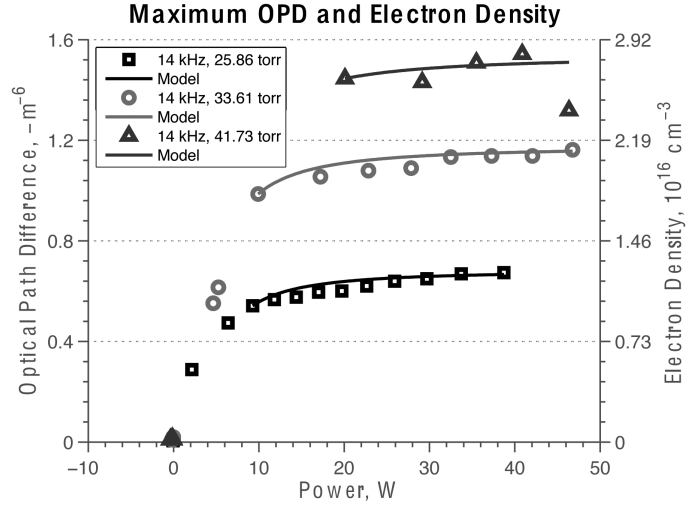
Fig. 13 Electron density and OPD as a function of plasma power. Curves correspond to the analytic model given by Equation 18.

lower pressures of 25.86 torr and 33.61 torr fall reasonably well on a straight line. At the higher pressure of 41.73 torr, the fewer number of data points makes it more difficult to assess. Averaging the two slopes at the lower pressures, the experimental constant was

$$K = -7.187 \times 10^{13}. \tag{20}$$

This was the value for K that was used in the model curve fits to the data in Figure 13.

The comparison between the electron density and OPD model, and experimental results was encouraging. At the lower two pressures, very good agreement was observed, particularly at higher voltages. At lower voltages, the model over-predicted the electron density. This is an indication that the power/electron density initiation values might be too high. Future work will attempt to pinpoint these locations with greater accuracy.

V.   Conclusions

This research investigated the feasibility of a "plasma lens" for wavefront control of light sources. The approach focused on the use of a dielectric barrier discharge (DBD) for the plasma generation. The wavefront distortion produced by the DBD generated plasma was characterized and related to the plasma electron density. The effect of gas pressure and plasma power were investigated.
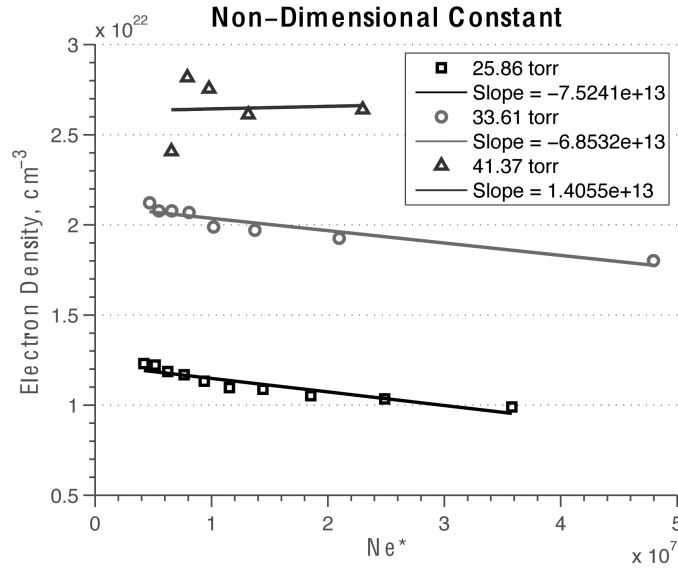
Fig. 14 Electron density, η_e, as a function η_e^* defined in Equation 19. Curves correspond to the analytic model given by Equation 18.

The results were compared to a derived analytic model for the electron density and optical path difference, OPD, as a function of the plasma power. The agreement between the experiment and analytic model was very good, especially at the higher plasma power levels. The maximum OPD increased with the gas pressure inside the "lens". A maximum OPD of approximately 1.5 μm was achieved in the experiment. This exceeds by an order of magnitude, the OPD values cited in aero-optic applications by Gordeyev et al[1], and otherwise corrected using electro-mechanical deformable mirrors. Notably, even larger OPD values can be achieved by using multiple devices in series. Air was used as the gas in the "plasma lens" for these feasibility experiments. Penning mixtures are preferable because they can be ionized at lower voltages than air. This will allow higher gas pressures to be used which will further increase the maximum possible OPD levels, and dynamic range. Future research will investigate the time response of the "plasma lens" which in theory should easily exceed that of electro-mechanical deformable mirrors.

References

[1] Gordeyev, S., Jumper, E., "Fluid Dynamics and Aero-Optical Environment Around Turrets," *40th AIAA Plasmadynamics and Lasers Conference,* AIAA, Washington, DC, 2009, AIAA Paper 2009-4224.

[2] Siegenthaler, J.P., Jumper, E.J, Gordeyev, S., "Atmospheric Propogation Vs. Aero-Optics," 46th AIAA Aerospace Sciences Meeting and Exhibit, Reno, NV, Jan. 2008, AIAA Paper 2008-1076.

[3] Mani, A., Wang, M., Moin, P., "Computational Study of Optical Distortions by Separated Shear Layers and Turbulent Wakes," *Journal of Fluid Mechanics*, Vol. 625, 2009, pp. 273-298.

[4] Becker, K.H., Kogelschatz, U., Schoenbach, K.H., Barker, R.J., "Non-Equilibrium Air Plasmas at Atmospheric Pressure," *Institute of Physics Publishing*, Philadelphia, PA, 2005.

[5] Enloe, C.L., McLaughlin, T.E., Font, G.I., Baughn, J.W., "Parameterization of Temporal Structure in the Single Dielectric Barrier Aerodynamic Plasma Actuator," *AIAA Journal*, Vol. 44, No. 6, Jun. 2006, pp. 1127-1137.

[6] Enloe, C.L., McLaughlin, T.E., Font, G.I., Baughn, J.W., "Frequency Effects on the Efficiency of the Aerodynamic Plasma Actuator," *44th AIAA Aerospace Sciences Meeting and Exhibit*, AIAA, Reno, NV, Jan. 2006, AIAA 2006-166.

[7] Corke, T.C., Enloe, C.L., Wilkinson, S.P., "Dielectric Barrier Discharge Plasma Actuators for Flow Control," *Annual Review of Fluid Mechanics*, Vol. 42, 2010, pp. 505-529.

[8] Enloe, C.L., et al., "Mechanisms and Responses of a Single Dielectric Barrier Plasma Actuator: Geometric Effects," *AIAA Journal*, Vol. 42, No. 3, Mar. 2004, pp. 595-604.

[9] Moreau, E., "Airflow Control by Non-Thermal Plasma Actuators," *Journal of Physics D: Applied Physics*, Vol. 40, Iss. 3, 2007, pp. 605-636.

[10] He, C., Corke, T.C., Patel, M.P., "Numerical and Experimental Analysis of Plasma Flow Control Over a Hump Model," *45th Aerospace Sciences Meeting*, AIAA, Reno, NV, Jan 2007, AIAA Paper 2007-0935.

[11] Boeuf, J.P., "Plasma Display Panels: Physics, Recent Developments, and Key Issues,", *Journal of Physics D: Applied Physics*, Vol. 36, 2003, pp. R53-R79.

[12] Max, C.E., Arons, J., Langdon, A.B., "Self-Modulation and Self-Focusing of Electromagnetic Waves in Plasmas," *Physical Review Letters*, Vol. 33, No. 4, Iss. 4, 1974, pp. 209-212.

[13] Buckingham, E., "On Physically Similar Systems: Illustrations of the Use of Dimensional Equations," Physical Review, Vol. 4, Iss. 4, 1914, pp. 345-376.

[14] Malacara, D., Thompson, B.J., "Handbook of Optical Engineering," *Marcel Dekker*, New York, NY, 2001.

[15] Born, M., Wolf, E., "Principles of Optics," *Cambridge University Press*, Cambridge, NY, 1999.